

Pramote Hochareon
Keefe B. Manning
Arnold A. Fontaine

Pennsylvania State University,
Department of Bioengineering,
205 Hallowell Building,
University Park, Pennsylvania 16802 USA

John M. Tarbell

City College of New York,
Department of Biomedical Engineering,
Convent Ave. @138th Street,
New York, New York 10031 USA

Steven Deutsch

Pennsylvania State University,
Department of Bioengineering,
205 Hallowell Building,
University Park, Pennsylvania 16802 USA

Fluid Dynamic Analysis of the 50 cc Penn State Artificial Heart Under Physiological Operating Conditions Using Particle Image Velocimetry

In order to bridge the gap of existing artificial heart technology to the diverse needs of the patient population, we have been investigating the viability of a scaled-down design of the current 70 cc Penn State artificial heart. The issues of clot formation and hemolysis may become magnified within a 50 cc chamber compared to the existing 70 cc one. Particle image velocimetry (PIV) was employed to map the entire 50 cc Penn State artificial heart chamber. Flow fields constructed from PIV data indicate a rotational flow pattern that provides washout during diastole. In addition, shear rate maps were constructed for the inner walls of the heart chamber. The lateral walls of the mitral and aortic ports experience high shear rates while the upper and bottom walls undergo low shear rates, with sufficiently long exposure times to potentially induce platelet activation or thrombus formation. In this study, we have demonstrated that PIV may adequately map the flow fields accurately in a reasonable amount of time. Therefore, the potential exists of employing PIV as a design tool. [DOI: 10.1115/1.1798056]

Keywords: PIV, Wall Shear Rate, Artificial Heart

I Introduction

Clot formation within an artificial heart is a major problem of device performance after implantation [1–3]. We hypothesize a strong connection between clot deposits on the sac wall of implanted artificial hearts with the underlying fluid dynamics within the chamber. Although the primary connection between the chamber flow field and the complex clotting process is not completely understood, the wall shear rate is a primary suspect. Many studies have been performed to investigate the relationship between wall shear rate and *in vivo* clot formation [4–6], with little closure. In the following, we describe the results of a particle image velocimetry (PIV) study in which the entire flow field of an artificial heart was mapped quite rapidly. We believe that this technique, when used in conjunction with recent work [7] on *in vivo* determination of clot formation in the same device, may go a long way toward clarifying the issue.

Artificial hearts have been successfully used clinically for more than a decade [8–11]. The current Penn State model, the “Lion-Heart” (Arrow International, Reading, PA), has a 70 cc fluid volume. Because of an increased demand for a smaller circulating volume device for use in smaller adults, a 50 cc artificial heart was introduced. This 50 cc chamber uses a scaled design of the 70 cc chamber.

The most complete study of the 70 cc heart flow field was performed by Baldwin et al. [12,13]. Baldwin et al. used laser Doppler anemometry (LDA) to obtain the mean velocity field and Reynolds stresses at 195 points in the chamber under physiological operating conditions. The highest velocities, 1.5–2.0 m/s, were found at the inlet and outlet ports near the valves. The flow in the main chamber formed a rotational pattern which filled the cham-

ber from the middle to the end of diastole. There were no significant separation regions observed. Other experimental studies of sac-type ventricles report a similar flow pattern [14,15].

Investigators have used several techniques [16–20], including flow visualization, dye washout, and pulsed Doppler ultrasound, to measure or infer wall shear stress within an artificial heart. Flow visualization and dye washout methods lead to qualitative measurements of wall shear stresses, and Doppler measurements only provide a limited area or a point by point measurement making entire planes time consuming to acquire. Flush-mounted hot-film anemometry, was done on an early pneumatic version of the Penn State heart by Baldwin et al. [21,22].

This device had a 100 cc chamber. Moreover, the angled inlet port was directed toward the center of the chamber, so that the overall diastolic rotational pattern found in the current 50 and 70 cc models was not observed. Wall shear stresses at 11 sites at the valve centerline of the chamber were measured. The results indicated that during diastole the wall shear stress reached a peak value of approximately 350 dynes/cm². The highest wall shear stresses were found near the aortic valve, for the case of 30% systolic duration, and were estimated to be as high as 2700 dynes/cm². Peak shear stress values of 1400 dynes/cm² were observed in the vicinity of the mitral valve. These results were dependent on the orientation of the hot-film relative to the flow direction. The hot-film technique is difficult to apply in artificial heart applications as it requires an external calibration and significant model modification. Moreover, since the hot-film is a heat transfer device, it is not very useful at low shear stresses.

Although clotting has not been a factor in the operation of the 70 cc device, which has been approved as a bridge to transplant in humans [3], there is good reason to be concerned about clot formation in smaller, scaled, devices. Animal experiments with a 15 cc version were unsuccessful, with explanted pumps showing ex-

Contributed by the Bioengineering Division for publication in the JOURNAL OF BIOMECHANICAL ENGINEERING. Manuscript received by the Bioengineering Division April 15, 2004; revision received May 4, 2004. Associate Editor: C. R. Ethier.

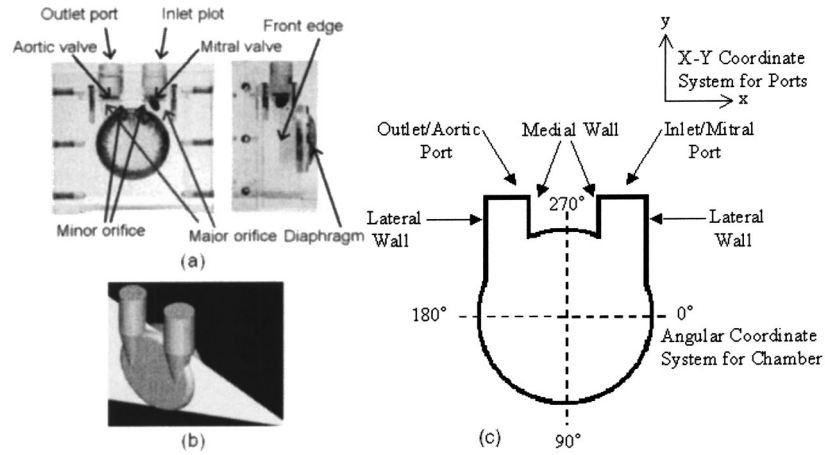


Fig. 1 50 cc Penn State artificial heart: (a) front and side view of the Plexiglas model; (b) light sheet orientation for the frontal plane (The light source shown here is placed from the inlet side, which is not necessarily true for all measurements.); and (c) coordinate systems: X-Y system for ports (straight surfaces) and angular system for chamber (curved surface)

tensive thrombus deposition within the pumping chamber. Bachmann et al. [2] have shown that the pediatric chamber has much lower wall shear rates and turbulent stresses than the adult device from which it is scaled. They note that some of these clotting problems may be associated with improper scaling of the inlet valve. Yamanaka et al. [7] have noted clot formation in *in vivo* animal studies of the geometrically scaled 50 cc heart. Such clot formation has not been observed in the 70 cc device.

Particle image velocimetry is used to measure the velocity field and estimate the wall shear rates in this study. While providing comparable spatial resolution to that obtained from LDA, PIV makes instantaneous, whole velocity field measurements available. This provides both the opportunity to calculate velocity derivatives and to study the structure of the overall flow field. One is able, for example, to calculate the fluid vorticity.

We have recently developed a PIV technique suitable for artificial heart application [23,24]. Raffel et al. published an excellent review of PIV: the concept, methodology, data processing, and post processing analysis [25]. A detailed theoretical background of PIV can be found in the work of Keane and Adrian [26,27].

II Methods

The 50 cc Penn State artificial heart test chamber, shown in Fig. 1(a) was made of transparent Plexiglas with a refractive index of 1.48. It was machined to be identical to the geometry of the front

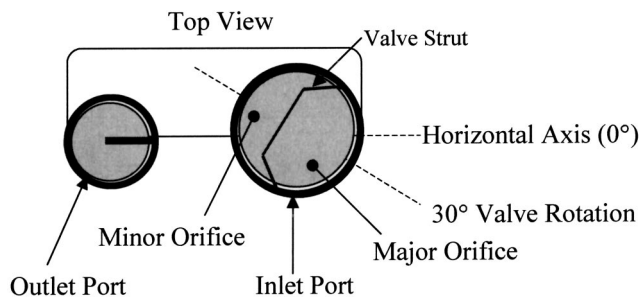


Fig. 2 A schematic detailing the orientation (30 deg rotation) of the 50 cc Penn State Artificial Heart's mitral valve

half of the implantable 50 cc artificial heart. The rear part of the chamber is covered by a flexible, polyurethane diaphragm fabricated with the same material used in the implantable artificial heart sac. The pusher-plate, which compressed the blood sac, was driven by a piston pump (Harvard Apparatus Co., Millis, MA). Bjork-Shiley (Shiley Inc., Irvine, CA) monostrut valves with pyrolytic carbon discs were used at the mitral (23 mm diameter) and aortic (21 mm diameter) ports, respectively, to achieve unidirectional flow.

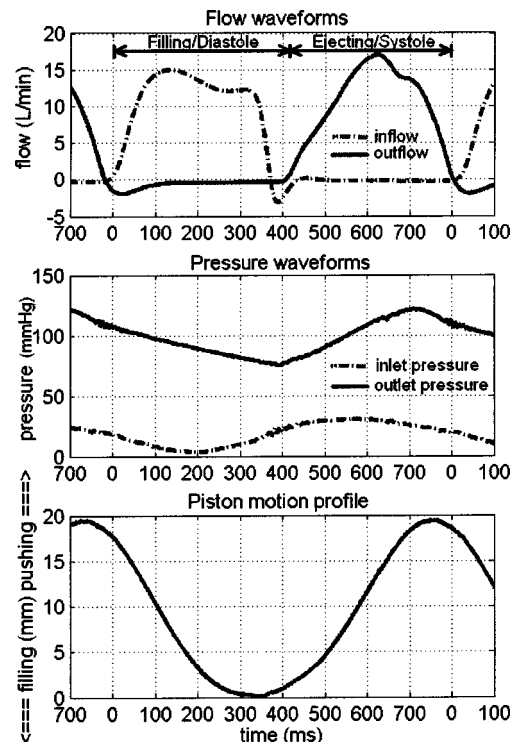


Fig. 3 Operating conditions (flow, pressure, and piston wave forms) for the experiments

To simulate physiological conditions, the artificial heart experiments were performed with a mock circulatory loop [28]. The inlet and outlet compliance chambers simulated the atrial and aortic compliance, respectively, while a parallel plate resistor downstream of the aortic compliance simulated the systemic resistance. A reservoir between the systemic resistance and the atrial compliance controlled the preload to the chamber. Pressure wave forms at the inlet and outlet compliance chambers were monitored by pressure transducers (Maxxim Medical, Athens, TX). Two ultrasonic flow meters (Transonic System Inc., Ithaca, NY) were used to record the flow wave forms at the inlet and outlet ports. The stroke length was monitored through the pusher-plate position as recorded by a linear velocity displacement transducer system (Solartron Metrology, West Sussex, UK).

The blood analog fluid was a mineral oil (Penreco Inc., Houston, TX), with a specific gravity of 0.827, refractive index of 1.46, and viscosity of 4.7 cP at room temperature. Red fluorescent coated 7 μm polystyrene particles (Duke Scientific Corp., Palo Alto, CA), with specific gravity of 1.055, were used for this experiment.

A dual pulsed Nd:YAG laser (New Wave Research, Fremont, CA) and appropriate cylindrical lens were used to form an approximately 1.5 mm thick light sheet to visualize the particles. A PIV synchronizer (TSI Inc., St. Paul, MN) with frame-grabber board (TSI Inc., St. Paul, MN) was used. Eighty PIV image pairs were recorded by a 1024 \times 1018 charge coupled device camera (TSI, Inc., St. Paul, MN) for each velocity field. The time marker for each beat cycle was referred to the pusher-plate position to minimize the beat-to-beat uncertainty of the time reference. An external triggering signal was generated by a signal delay toolbox, which has a time increment of 0.1 ms. Figure 1(b) shows the light sheet orientation. The light plane was 5 mm away from the front edge, near the centerline of the chamber. The chamber was 18.8 mm wide. The light source was placed on the side of the heart at which the measurements were taken. Note that the valve is rotated 30 deg, as shown in Fig. 2, and the light sheet plane is not located at peak inflow.

Cross-correlation of the images was performed by the TSI INSIGHT 5 software. A recursive or multigrid cross-correlation scheme was used with an initial interrogation window of 64 \times 64 pixels, stepped down by a factor of two to reach the final interrogation window of 16 \times 16 pixels [29,30]. The final 16 \times 16 pixel interrogation size was selected to achieve a minimum of four particles per interrogation window [25–27] and an optimal interrogation window size for first order accurate wall shear-rate calculations, as based on earlier results [23]. A Hart correlation, cross-correlation based correction with sparse array compressed image correlation [31–33], was selected with a bilinear peak finding algorithm. Each interrogation window has 50% overlapping with its neighbors. Non-fluid areas were digitally masked to prevent anomalies in the Plexiglas model from influencing the cross-correlation [24].

Eight local areas (medial and lateral walls of the mitral and aortic ports and the right, bottom, left, and top walls of the curved chamber) within the 50 cc chamber were investigated in addition to the entire chamber view. The time separations were optimized for each measurement (location and time) to achieve a maximum particle displacement of one fourth of the primary interrogation window size [25,27], 64 pixels in our measurements. The image magnification and interrogation region size were selected to minimize variation in the maximum particle displacement between adjacent final interrogation windows to approximately two to four pixels. This was done to ensure that the displacement gradient across the two windows is small when using the Hart cross correlation correction [34]. For the global view of the artificial heart chamber and for the local areas within the artificial heart, magnifications of 85 $\mu\text{m}/\text{pixel}$ and approximately 25 $\mu\text{m}/\text{pixel}$ were achieved, respectively.

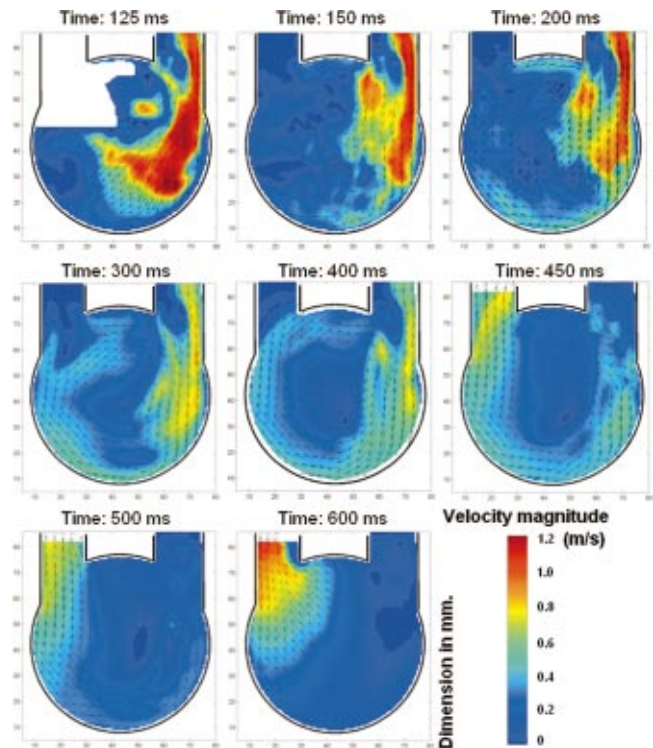


Fig. 4 The PIV velocity maps during early diastole (125 and 150 ms), middle to late diastole (200–400 ms), and systole (450–600 ms) for the 50 cc Penn State artificial heart (Time reference is from the onset of diastole)

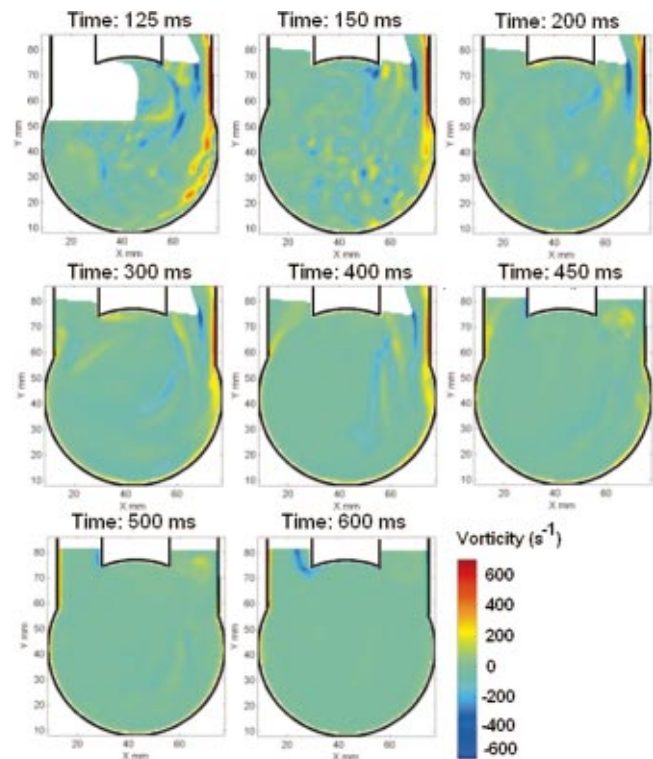


Fig. 5 The vorticity maps during early diastole (125 and 150 ms), middle to late diastole (200–400 ms), and systole (450–600 ms) for the 50 cc Penn State artificial heart

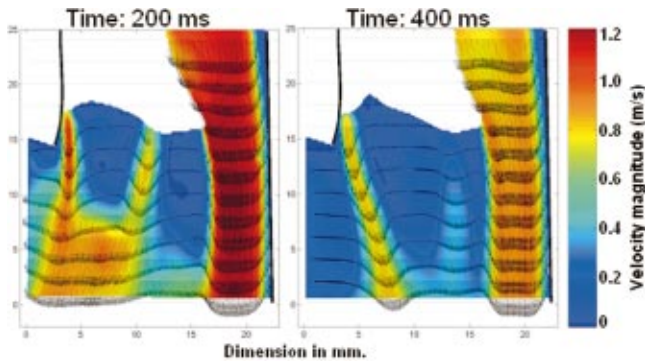


Fig. 6 The velocity maps of the mitral port at 200 and 400 ms for the 50 cc Penn State artificial heart

A range and local median validation criteria [35] were sequentially used for each vector file obtained from INSIGHT 5. The exact tolerance values (approximately 80%) for each criterion were manually adjusted to obtain reasonable results. Invalid instantaneous vector fields were manually excluded. For the remaining valid vector files, no interpolation and no smoothing has been applied to avoid error propagation from the neighboring vector. Averaging was performed vector-by-vector to obtain the ensemble mean velocity field as a function of space and time.

The components of the two-dimensional velocity gradient were calculated by central differencing, which is second-order accurate

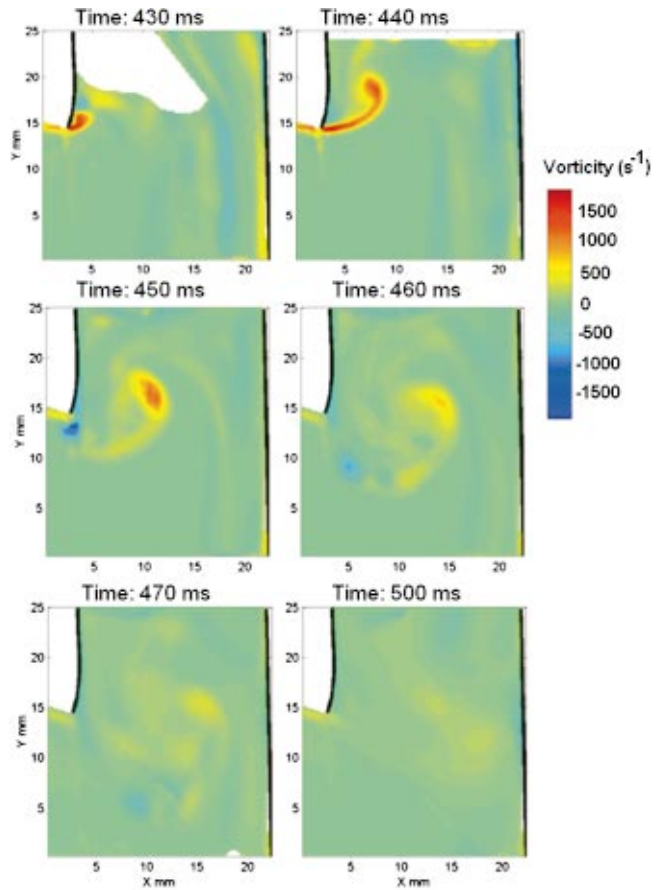


Fig. 8 The vorticity maps of the mitral port area from 430, 440, 450, 460, 470, and 500 ms for the 50 cc Penn State artificial heart

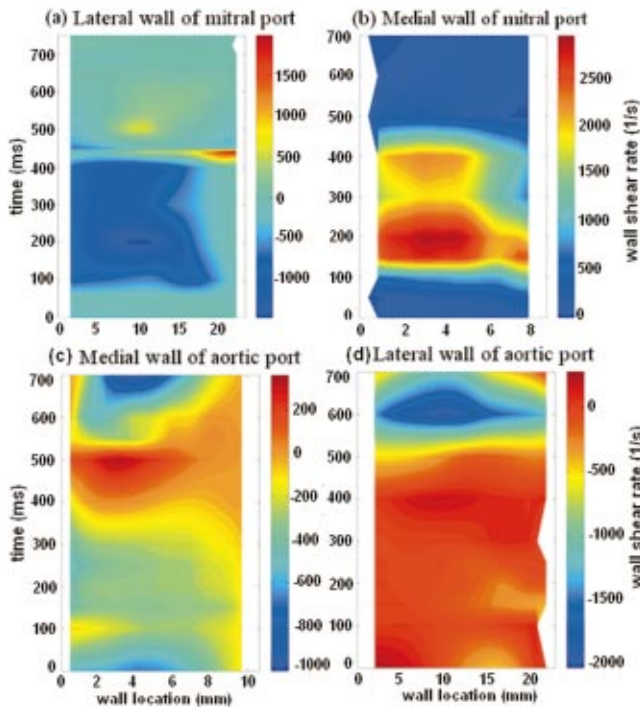


Fig. 7 The inlet/outlet ports' average wall shear rate in time series in the beat cycle from (a) the lateral wall of the mitral port (The fully open valve tip position is at wall location approximately 16 mm.), (b) the medial wall of the mitral port (The fully open valve tip position is at wall location approximately 8 mm.), (c) the medial wall of the aortic port, and (d) the lateral wall of the aortic port of the 50 cc Penn State artificial heart

[25]. Vorticity fields were subsequently calculated from the velocity gradient. In the figures, positive vorticity is a counter-clockwise rotation. Wall shear-rate calculations were performed by a wall coordinate decomposition of the near wall velocity vectors and a first-order, one-sided differencing of the tangential velocity component, in conjunction with the no-slip boundary condition at the wall. Details of the wall shear rate calculation may be found in Hochareon et al. [23]. The inlet and outlet port coordinate system (x - y system) and the chamber wall coordinate system (angular) are shown in Fig. 1(c).

Operating conditions for the mock circulation loop are shown in Fig. 3, with an average flow rate of 4.72 liters/min, stroke length of 19.4 mm, stroke volume of 62.93 cc, and heart rate of 75 beats/min. Note that diastole, filling, starts at 0 ms, and systole begins at 430 ms. Hochareon et al. [36] have shown that the sac opens non-uniformly with the bottom opening first.

III Results

A Global Flow Field. The average flow maps throughout the beat cycle are shown in Fig. 4, and vorticity maps are shown in Fig. 5. Figures 4 and 5 include data for early diastole (125 and 150 ms), middle to late diastole (200 to 400 ms), and systole (450 to 600 ms). The peak flow is approximately 1.2 m/s and occurs both in diastole and systole, at the major orifice of both the mitral and aortic ports, respectively. This maximum velocity is the same order as that observed by Baldwin et al. [13]. During early dias-

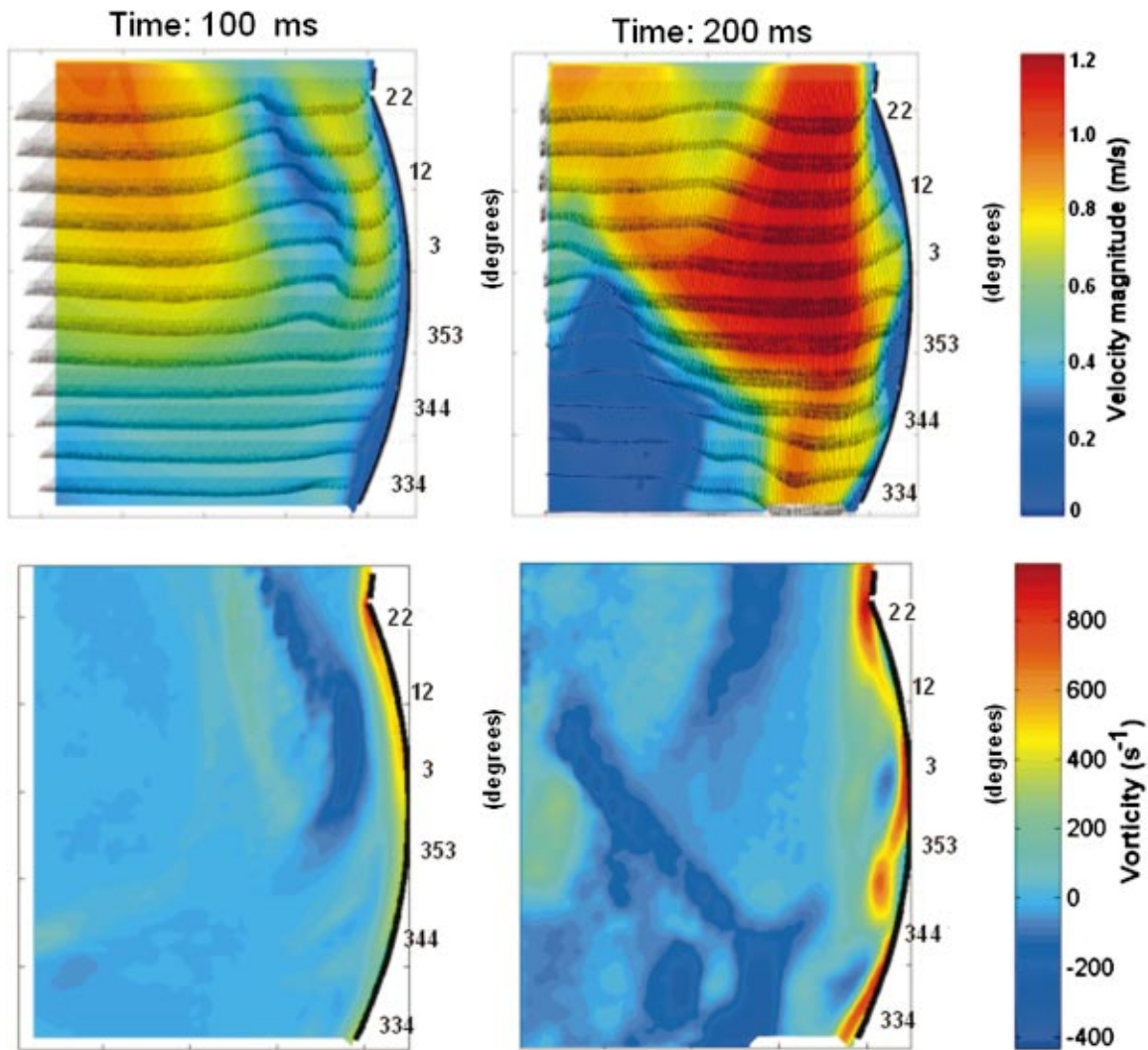


Fig. 9 The velocity and vorticity maps of the right wall from 100 and 200 ms for the 50 cc Penn State artificial heart. (Note: The size of area is 30×30 mm.)

tole, as shown in Fig. 4, an inflow jet from the mitral port rapidly fills the bottom part of the chamber. The vorticity maps show the development of the wall boundary layer and some small-scale flow patterns in the main chamber which occur during the transient phase of early diastole, 125 and 150 ms, as shown in Fig. 5. During late diastole, the flow within the main chamber forms a rotational flow pattern (Fig. 4 at 300 and 400 ms) similar to that reported by Baldwin [13] for the 70 cc Penn State artificial heart chamber.

Systole starts when the mitral valve closes and the aortic valve opens, which is at 450 ms. The rotational flow remains through the transient phase of very early systole and then rapidly disappears. Near 500 ms, the overall flow in the main chamber changes direction toward the outlet port. The peak outflow at the aortic port is at 600 ms as shown in Fig. 4.

B Local Flow Fields. The local flow field near the mitral port at 200 ms, shown in Fig. 6, reveals details of the flow structure of the inflow jet. This jet remains throughout diastole, but with decreasing velocity as shown in Fig. 6 at 400 ms. The jet creates high wall shear rates with a magnitude of 500–1500 s^{-1} on the lateral wall of the mitral port during diastole, as shown in Fig. 7(a). The wall shear rate is shown to change sign at most wall locations, which may indicate short periods of local separation,

just before the start of systole (450 ms). Peak stresses occur near this time also, although they have only a small spatial/temporal extent.

We observe a secondary inflow jet in the minor orifice of the mitral port (Fig. 6) through diastole. Figure 6 shows the secondary jet flow on the minor orifice during mitral valve opening. The jet magnitude is of the same order as that of the major orifice jet and since its flow axis lies very close to the wall, this jet creates significant wall shear on the medial wall of the mitral port. The wall shear rate map for the medial wall, as shown in Fig. 7(b), shows the wall shear rates with magnitudes of approximately 1000–3000 s^{-1} , which is roughly twice as high as those of on the lateral wall. There are two temporal regions of peak wall shear rate, and this is probably related to the double peak in the inflow waveform as shown in Fig. 3.

As the valve closes, a separation region on the medial wall of the mitral port forms. In Fig. 8, we observe a closing vortex, created at the corner of the medial wall of the mitral port and the upper wall of the chamber, which follows the motion of the valve. On the lateral wall [Fig. 7(a)], there is a high shear rate region with a magnitude of almost 2000 s^{-1} , near the wall location of 20 mm. This high shear rate corresponds to the high ve-

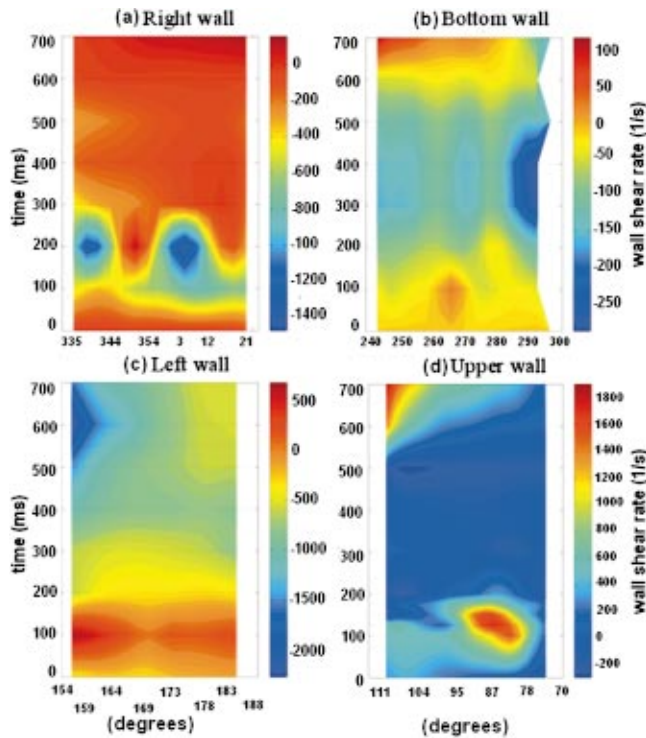


Fig. 10 The chamber's average wall shear rate in time series in the beat cycle from (a) the right wall, (b) the bottom wall, (c) the left wall, and (d) the upper wall of the 50 cc Penn State artificial heart

locity flow structure at the very top region near the lateral wall (Fig. 6). This is related to the regurgitant flow first studied by Baldwin et al. [12].

Systole begins after mitral valve closure at 450 ms through to 800 ms (Fig. 3). From time 440 to 470 ms (Fig. 8), the mitral valve closing vortex creates another high shear rate spot with a magnitude of approximately 1200 s^{-1} on the medial wall. The progression of the closing vortex is shown in Fig. 8.

From Fig. 4, we might expect a separation region below the transition from the lateral wall of the mitral port to the main chamber, where the inflow jet appears to detach. High-resolution flow maps of the right wall of the artificial heart show two small low-velocity areas near the wall at the time 200 ms, in Fig. 9. However, a higher magnification view (not shown), made using a particle tracking technique, indicates no strong evidence of a detached boundary layer at 200 and 300 ms [24]. The vorticity maps, also provided in Fig. 9, show that the shear layer remains attached at 100 ms, and starts to detach from the wall at 200 ms. Shown in Fig. 10(a) is the shear rate map from the right wall of the chamber [near 0 deg in Fig. 1(c)]. It shows wall shear rates with magnitudes of $700\text{--}1000 \text{ s}^{-1}$ at the time 100 ms. At 200 ms, there are two areas of low wall shear rates corresponding to the low-velocity areas. Near 353 deg, the area has an opposite wall shear rate direction, indicating a flow separation. The peak wall shear rate, however, increases in magnitude to 1400 s^{-1} at 200 ms. This wall shear rate profile approaches zero at times greater than 300 ms. During 300 to 400 ms, there is a very low shear rate area at 12 deg [Fig. 10(a)]. In systole, the wall shear rates have lower magnitude, and the flow starts changing direction after 600 ms, as the wall shear rate becomes positive, but yet remains at low magnitude.

Magnified views in Fig. 11 of the bottom region show a thick low velocity area, which might indicate flow separation, during

middle to late diastole and early systole. The vorticity fields from 200 and 300 ms, also shown in Fig. 11, reveal the shear layer is detached from the wall. The shear rate map [Fig. 10(b)] for this region indicates low wall shear rate for the entire cycle ranging from $0\text{--}250 \text{ s}^{-1}$.

At time 100 ms, the diaphragm obstructs the light source in the global view hiding a flow structure near the outlet port that becomes visible with the higher magnification. The shear rate map, given in Fig. 10(c) [near 180 deg in Fig. 1(c)], shows that the wall shear rate changes sign near 200 ms. Through systole, we observe a patch of very high shear rate at a location nearest the aortic port. During diastole, we observe the regurgitant jet after aortic valve closure, first observed by Baldwin et al. [13]. This regurgitant jet lasts for almost the entire period of aortic valve closure, 100 to 300 ms, and creates wall shear rates of $300\text{--}400 \text{ s}^{-1}$, on the medial wall as shown in Fig. 7(c).

During systole, a separation region is progressively formed on the medial wall of the aortic port from the beginning of systole, continuing through 700 ms. This region was not measured in the Baldwin et al. LDA results [13]. The vorticity maps show the progressive detachment of the shear layer from the medial wall. The wall experiences near zero shear rate through diastole [Fig. 7(d)]. High shear rates start with the onset of systole and reaches a peak of 2000 s^{-1} at 600 ms.

The upper region of the chamber is the most affected by the diaphragm motion, as it corresponds to the area of the diaphragm with the most nonuniform opening pattern [36]. The shear rate map [Fig. 10(d)] reveals very low wall shear rates, magnitudes less than 200 s^{-1} , throughout almost the entire cycle and spatial extent.

IV Discussion

This PIV study has located areas of high and low shear rates that may have a propensity for hemolysis or platelet activation and thrombus formation. In addition, the study presents data on areas not previously reported such as the medial walls of the mitral and aortic ports and the upper part of the heart chamber. Figure 12 provides a qualitative overview of the wall shear rates during diastole and systole.

During diastole, high shear rate zones occur mainly near the mitral port. Previous LDA work that described the lateral wall high shear rate zone [13] has been confirmed here [Fig. 7(a)], but, PIV has revealed that the medial wall of the mitral port [Fig. 7(b)] also experiences a high shear rate zone. In this particular planar location, the shear rate appears to be greater along the medial wall as compared to the lateral wall. This may be significant for hemolysis and platelet activation since the high shear rate appears to last for approximately 100 ms. A moderate to high shear rate zone is present along the left side of the heart during diastole a result of the fluid entering the chamber and setting up a rotating flow pattern. Two low flow areas are identified as significant to potential thrombus formation. The bottom wall [Fig. 10(b)] is of particular interest since there has been some evidence of clot formation seen *in vivo* [7] near this particular area. The top of the chamber or upper wall [Fig. 10(d)] is also described as a low shear rate area. This area has not been investigated previously, and the results suggest a potential risk for thrombus formation as the low shear rate occurs for over 300 ms. At the onset of diastole, a brief high shear rate area appears which could provide washout or more importantly, remove any deposits. To this point there is no *in vivo* data to indicate any evidence of clots located in this region.

During the systolic phase, high shear rate areas exist along the left wall of the heart chamber near the aortic port [Fig. 10(c)] and along the lateral wall of the aortic port [Fig. 7(d)]. This is to be expected since the major orifice of the mechanical heart valve is oriented along the lateral wall and would experience a high vol-

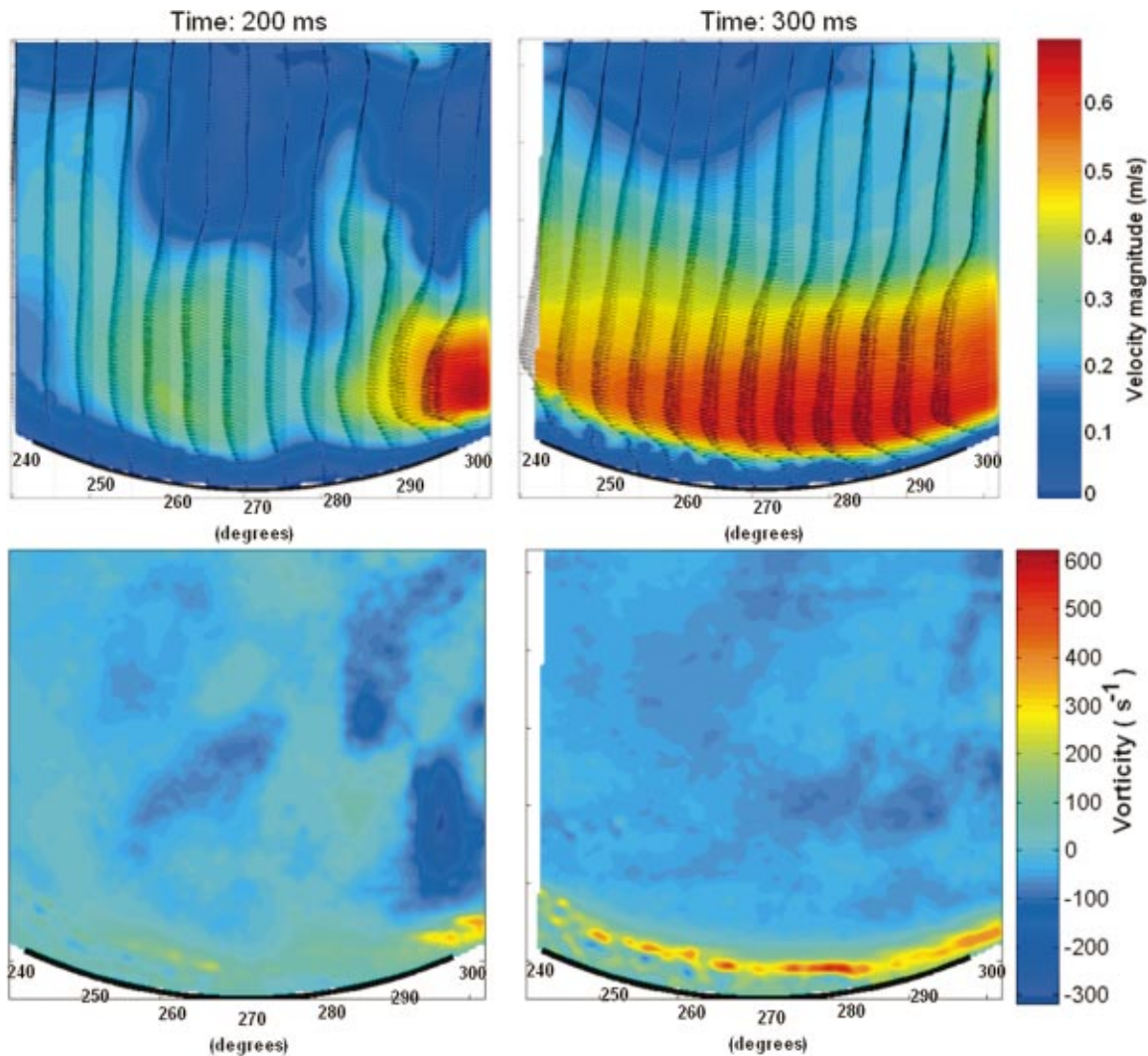


Fig. 11 The velocity and vorticity maps of the bottom wall from time 200 and 300 ms for the 50 cc Penn State artificial heart. (Note: The size of area is 30×30 mm.)

ume of fast moving fluid. Even more intriguing about the aortic port flow field has to be the low wall shear rates along the medial wall [Fig. 7(c)]. Unlike its mitral port counterpart, the aortic port experiences low wall shear rates suggesting a potential area for deposition.

Perhaps the most fascinating results are the low wall shear rates at the top and bottom of the chamber. These areas experience low flow zones throughout the entire cycle (both diastole and systole) that suggest a separation from the bulk flow. Should the local residence time be appropriate, the clotting cascade could be initiated resulting in deposition on the chamber. Although during the latter part of diastole there is a rotational flow pattern of the bulk flow, this flow pattern may not provide adequate washout at the top and bottom of the chamber allowing clots to form.

The most complete study of shear rates in an artificial heart was conducted by Baldwin et al. [21] and Baldwin [22], using hot film probes in a 100 cc model. Comparison with their results are not direct as the Baldwin et al. model had an angled central inlet port that did not produce the same global rotational motion observed in the current 50 and 70 cc models. The reduction in stroke volume (50 from 100) and the lower flow rate (4.72 l/min from 6) may inherently reduce wall shear rates. In addition, the mitral valve

was rotated 30 deg here, so that the light sheet was not in line with the peak inflow, while the Baldwin et al. probes were oriented along the centerline of his valves. However, it is clear that smaller wall shear stresses are generally observed in the 50 cc heart.

V Conclusion

Particle image velocimetry measurements were used to create a two-dimensional view of the entire 50 cc artificial heart flow field as a function of time. Critical features such as the inlet jet and valve closing vortices were quantified. In addition, we were able to calculate the wall shear rate profiles, as a function of time, for the interior walls of the chamber. As the 50 cc pump has been observed to clot, *in vivo*, a particularly interesting result is the low shear rates at the top and bottom of the chamber throughout the flow cycle. A comparison of wall shear rates against clot formation is now possible, and would be extremely useful. The study shows further, that with affordable experimental and analytical effort, a fluid dynamic study of the artificial heart under differing operating conditions, to better simulate the natural environment that the implanted hearts experience, is achievable.

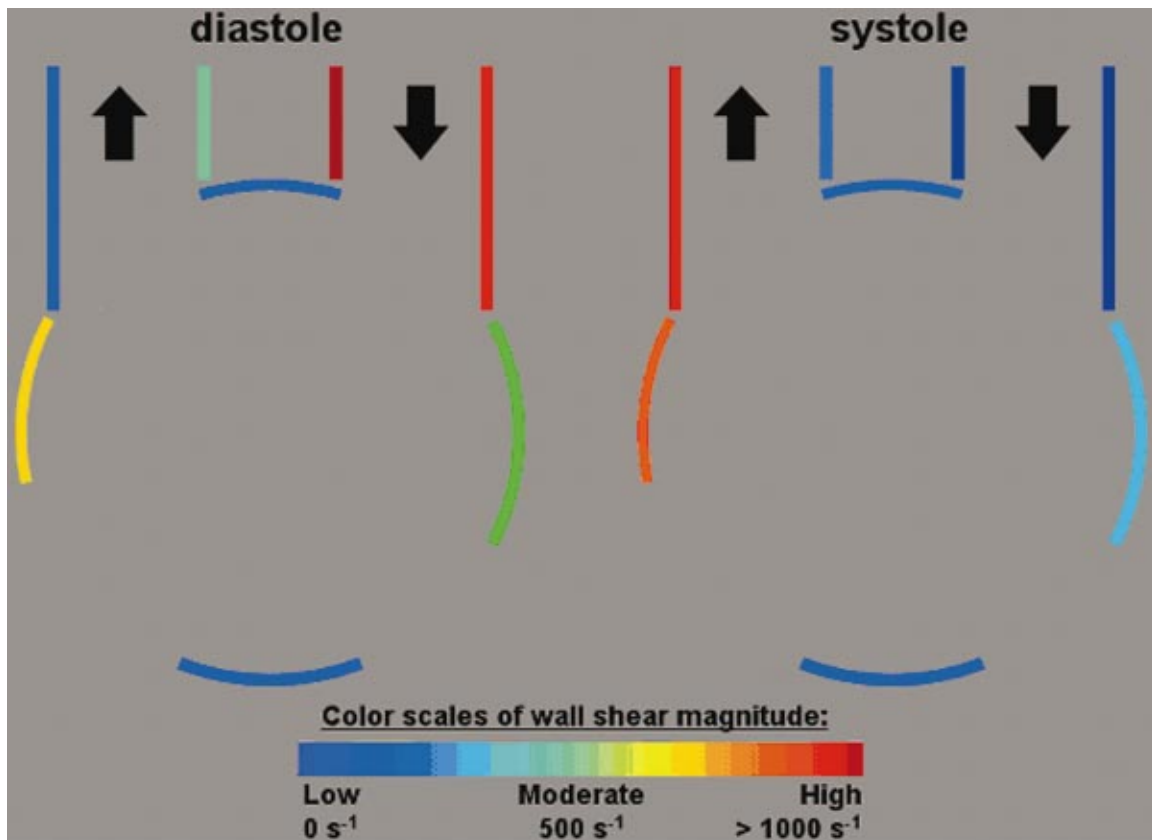


Fig. 12 Qualitative summary of wall shear rates within the 50 cc Penn State artificial heart during diastole and systole

Acknowledgment

This research was supported through the NIH through Grant No. HL60276.

References

- [1] DeVries, W. C., Anderson, J. L., Joyce, L. D., Anderson, F. L., Hammond, E. H., Jarvik, R. K., and Kolff, W. J., 1984, "Clinical Use of the Total Artificial Heart," *N. Engl. J. Med.*, **310**, pp. 273–278.
- [2] Bachmann, C., Hugo, G., Rosenberg, G., Deutsch, S., Fontaine, A., and Tarbell, J. M., 2000, "Fluid Dynamics of a Pediatric Ventricular Assist Device," *Artif. Organs*, **24**, pp. 362–372.
- [3] Magovern, J. A., Pennock, J. L., Campbell, D. B., Pae, Jr., W. E., Pierce, W. S., and Waldhausen, J. A., 1986, "Bridge to Heart Transplantation: The Penn State Experience," *J. Heart Transplant*, **5**, pp. 196–202.
- [4] Orvim, U., Barstad, R. M., Orning, L., Petersen, L. B., Ezban, M., Hedner, U., and Sakariassen, K. S., 1997, "Antithrombotic Efficacy of Inactivated Active Site Recombinant Factor VIIa is Shear Dependent in Human Blood," *Arterioscler., Thromb., Vasc. Biol.*, **17**, pp. 3049–3056.
- [5] Holme, P. A., Orvim, U., Hamers, M. J., Solum, N. O., Brosstad, F. R., Barstad, R. M., and Sakariassen, K. S., 1997, "Shear-Induced Platelet Activation and Platelet Microparticle Formation at Blood Flow Conditions as in Arteries with a Severe Stenosis," *Arterioscler., Thromb., Vasc. Biol.*, **17**, pp. 646–653.
- [6] Badimon, L., Badimon, J. J., Galvez, A., Chesebro, J. H., and Fuster, V., 1986, "Influence of Arterial Damage and Wall Shear Rate on Platelet Deposition. Ex Vivo Study in a Swine Model," *Arteriosclerosis (Dallas)*, **6**, pp. 312–320.
- [7] Yamanaka, H., Rosenberg, G., Weiss, W. J., Snyder, A. J., Zapanta, C. M., Pae, W. E., and Siedlecki, C. A., 2003, "A Multiscale Surface Evaluation of Thrombosis in Left Ventricular Assist Systems," *ASAIO J.*, **49**, pp. 222.
- [8] Weiss, W. J., Rosenberg, G., Snyder, A. J., Pierce, W. S., Pae, W. E., Kuroda, H., Rawhouser, M. A., Felder, G., Reibson, J. D., Cleary, T. J., Ford, S. K., Marlotte, J. A., Nazarian, R. A., and Hicks, D. L., 1999, "Steady State Hemodynamic and Energetic Characterization of the Penn State/3M Health Care Total Artificial Heart," *ASAIO J.*, **45**, pp. 189–193.
- [9] Weiss, W. J., Rosenberg, G., Snyder, A. J., Donachy, Sr., J., Reibson, J., Kawaguchi, O., Sapirstein, J. S., Pae, W. E., and Pierce, W. S., 1993, "A Completely Implanted Left Ventricular Assist Device: Chronic In Vivo Testing," *ASAIO J.*, **39**, pp. M427–M432.
- [10] Davis, P. K., Pae, W. E., and Pierce, W. S., 1989, "Toward an Implantable Artificial Heart: Experimental and Clinical Experience at The Pennsylvania State University," *Invest. Radiol.*, **24**, pp. 81–87.
- [11] Mavroidis, D., Sun, B. C., and Pae, W. E., 1999, "Bridge to Transplantation: The Penn State Experience," *Ann. Thorac. Surg.*, **68**, pp. 684–687.
- [12] Baldwin, J. T., 1990, "An Investigation of the Mean Fluid Velocity and Reynolds Stress Fields with an Artificial Heart Ventricle," Ph.D. thesis, The Pennsylvania State University, University Park, PA.
- [13] Baldwin, J. T., Deutsch, S., Geselowitz, D. B., and Tarbell, J. M., 1994, "LDA Measurements of Mean Velocity and Reynolds Stress Fields within an Artificial Heart Ventricle," *ASME J. Biomech. Eng.*, **116**, pp. 190–200.
- [14] Jin, W., and Clark, C., 1993, "Experimental Investigation of Unsteady-Flow Behavior within a Sac-Type Ventricular Assist Device (VAD)," *J. Biomech.*, **26**, pp. 697–707.
- [15] Jin, W., and Clark, C., 1994, "Experimental Investigation of the Motions of the Pumping Diaphragm within a Sac-Type Pneumatically Driven Ventricular Assist Device," *J. Biomech.*, **27**, pp. 43–55.
- [16] Phillips, W. M., Brighton, J. A., and Pierce, W. S., 1972, "Artificial Heart Evaluation Using Flow Visualization Techniques," *Trans. ASAIO*, **18**, pp. 194–201.
- [17] Mann, K. A., 1985, "Fluid Dynamic Analysis of Newtonian and Non-Newtonian Fluids in a Penn State Ventricular Assist Device," M.S. thesis, The Pennsylvania State University, University Park, PA.
- [18] Affeld, A., 1979, *The State of the Art of the Berlin Total Artificial Heart—Technical Aspects*, Assisted Circulation, edited by F. Unger, Springer-Verlag, New York, pp. 307–333.
- [19] Tarbell, J. M., Gunshinan, J. P., Geselowitz, D. B., Rosenberg, G., Shung, K. K., and Pierce, W. S., 1986, "Pulsed Ultrasonic Doppler Velocity Measurements Inside a Left Ventricular Assist Device," *ASME J. Biomech. Eng.*, **108**, pp. 232–238.
- [20] Phillips, W. M., Furkay, S. S., and Pierce, W. S., 1979, "Laser Doppler Anemometer Studies in Unsteady Ventricular Flows," *Trans. ASAIO*, **25**, pp. 56–60.
- [21] Baldwin, J. T., Tarbell, J. M., Deutsch, S., Geselowitz, D. B., and Rosenberg, G., 1988, "Hot-Film Wall Shear Probe Measurements Inside a Ventricular Assist Device," *ASME J. Biomech. Eng.*, **110**, pp. 326–333.
- [22] Baldwin, J. T., 1987, "Wall Shear Stress Measurements in the Penn State Ventricular Assist Device Using Hot-Film Anemometry," M.S. thesis, Pennsylvania State University, University Park, PA.
- [23] Hochareon, P., Manning, K. B., Fontaine, A. A., Deutsch, S., and Tarbell, J. M., 2003, "Wall Shear-Rate Estimation within the 50cc Penn State Artificial Heart Using Particle Image Velocimetry," *J. Biomech. Eng.*, (to be published).

- [24] Hochareon, P., 2003, "Development of Particle Imaging Velocimetry (PIV) for Wall Shear Stress Estimation within a 50cc Penn State Artificial Heart Ventricular Chamber," PhD thesis, Pennsylvania State University, University Park, PA.
- [25] Raffel, M., Willert, C. E., and Kompenhans, J., 1998, *Particle Image Velocimetry: A Practical Guide*, Springer-Verlag, Berlin.
- [26] Keane, R. D., and Adrian, R. J., 1992, "Theory of Cross-Correlation Analysis of PIV Images," *Appl. Sci. Res.*, **49**, pp. 191–215.
- [27] Adrian, R. J., 1991, "Particle-Imaging Techniques for Experimental Fluid-Mechanics," *Annu. Rev. Fluid Mech.*, **23**, pp. 261–304.
- [28] Fikse, T. H., Rosenberg, G., Snyder, A. J., Landis, D. L., Hanson, K. L., Kern, S. E., Geselowitz, D. B., and Pierce, W. S., 1984, "Development and Verification of EVAD/Mock Loop System Model," *Frontiers of Engineering and Computing in Health Care, 1984, Proceedings, Sixth Annual Conference*, IEEE Engineering in Medicine and Biology Society, Los Angeles, CA.
- [29] Scarano, F., and Riethmuller, M. L., 1999, "Iterative Multigrid Approach in PIV Image Processing with Discrete Window Offset," *Exp. Fluids*, **26**, pp. 513–523.
- [30] Scarano, F., and Riethmuller, M. L., 2000, "Advances in Iterative Multigrid PIV Image Processing," *Exp. Fluids*, **29**, pp. S51–S60.
- [31] Hart, D. P., 1998, "High-Speed PIV Analysis Using Compressed Image Correlation," *ASME J. Fluids Eng.*, **120**, pp. 463–470.
- [32] Hart, D. P., 1999, "Super-Resolution PIV by Recursive Local-Correlation," *J. Visualization*, **10**, pp. 1–10.
- [33] Hart, D. P., 1998, "The Elimination of Correlation Errors in PIV Processing," *9th International Symposium on Applications of Laser Techniques to Fluid Mechanics*, Lisbon, Portugal, Instituto Superior Técnico, Lisbon, Portugal, July 13–16, 1998.
- [34] Hart, D. P., 2000, "PIV Error Correction," *Exp. Fluids*, **29**, pp. 13–22.
- [35] J Westerweel, J., 1994, "Efficient Detection of Spurious Vectors in Particle Image Velocimetry Data," *Exp. Fluids*, **16**, pp. 236–247.
- [36] Hochareon, P., Manning, K. B., Fontaine, A. A., Deutsch, S., and Tarbell, J. M., 2003, "Diaphragm Motion Affects Flow Patterns in an Artificial Heart," *Artif. Organs*, **27**, pp. 1102–9.
- [37] Bachmann, C., Hugo, G., Rosenberg, G., Deutsch, S., Fontaine, A., and Tarbell, J. M., 2000, "Fluid Dynamics of a Pediatric Ventricular Assist Device," *Artif. Organs*, **24**, pp. 362–372.